Elastic behavior of MFI-type zeolites: 3 – Compressibility of silicalite and mutinaite

Elastic behavior of MFI-type zeolites: 3 – Compressibility of silicalite and mutinaite

Simona Quartieri[a,*] Rossella Arletti[b], Giovanna Vezzalini[c], Francesco Di Renzo[d], Vladimir Dmitriev[e]

[a]Dipartimento di Scienze della Terra, Università di Messina, Viale Ferdinando Stagno d'Alcontres 31, 98166 Messina S. Agata, Italy

[b]Dipartimento di Scienze Mineralogiche e Petrologiche, Via Valperga Caluso 35, 10125 Torino, Italy

[c]Dipartimento di Scienze della Terra, Università di Modena e Reggio Emilia, Via S. Eufemia 19, 41100 Modena, Italy

[d]Institut Charles Gerhardt de Montpellier, UMR 5253 CNRS-UM2-ENSCM-UM1, 8 rue Ecole Normale, 34296 Montpellier, France

[e]Swiss–Norwegian Beam Line at ESRF, BP220, 38043 Grenoble Cedex, France

Abstract

We report the results of an in-situ synchrotron X-ray powder diffraction study – performed using silicone oil as "non-penetrating" pressure transmitting medium – of the elastic behavior of three zeolites with MFI-type framework: the natural zeolite mutinaite and two silicalites (labeled A and B) synthesized under different conditions. While in mutinaite no symmetry change is observed as a function of pressure, a phase transition from monoclinic ($P2_1/n$) to orthorhombic (Pnma) symmetry occurs at about 1.0 GPa in the silicalite samples. This phase transition is irreversible upon decompression. The second order bulk moduli of silicalite A and silicalite B, calculated after the fulfillment of the phase transition, are: K_0=18.2(2) and K_0=14.3 (2) GPa, respectively. These values makes silicalite the most compressible zeolite among those up to now studied in silicone oil. The structural deformations induced by HP in silicalite A were investigated by means of complete Rietveld structural refinements, before and after the phase transition, at P_{amb} and 0.9 GPa, respectively. The elastic behaviors of the three MFI-type zeolites here investigated were compared with those of Na-ZSM-5 and H-ZSM-5, studied in similar experimental conditions: the two silicalites – which are the phases with the highest Si/Al ratios and hence the lowest extraframework contents – show the highest compressibility. On the contrary, the most rigid material is mutinaite, which has a very complex extraframework composition characterized by a high number of cations and water molecules.

Graphical abstract

High-pressure behavior of silicalite compressed in silicone oil: projection of the structure along the [0 1 0] direction at Pamb(a), 0.9 GPa (b). (c) Comparison of the unit-cell volume variations as a function of pressure for mutinaite, H-ZSM5, Na-ZSM5, silicalite A, and silicalite B compressed in silicone oil.

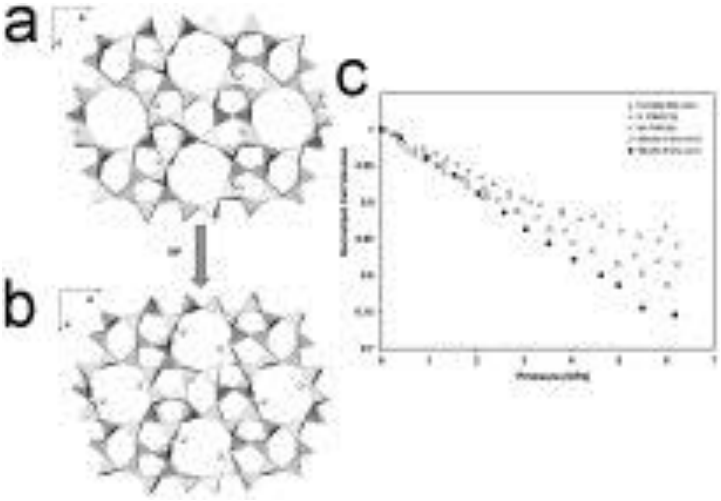

* Corresponding author. E-mail address: squartieri@unime.it (S. Quartieri).

Highlights

X-ray powder diffraction study of silicalite and mutinaite compressibility.

Silicalite is the most compressible zeolite up to now studied.

A phase transition from monoclinic to orthorhombic symmetry occurs in silicalite.

Among MFI-type zeolites the most rigid material is mutinaite.

Keywords

- Zeolite;
- Silicalite;
- Mutinaite;
- High pressure;
- Elastic behavior;
- Synchrotron X-ray powder diffraction

1. Introduction

MFI-type porous materials comprise both the rare natural zeolite mutinaite [1] and several synthetic phases of wide industrial interest as shape-selective catalysts and selective adsorbers (like e.g., ZSM-5 [2] and [3]). This zeolite topology is also that of the all-silica phase called silicalite [4] and [5]. The applicative importance of MFI-type zeolites is due to their unique structure [2] and [3], consisting of intersecting channels formed by 10 $(Al,Si)O_4$ tetrahedra with a mean diameter of 5–6 Å, obtained by the linking of 5-membered rings chains. The channels (Fig. 1) are linear in the *b* direction and sinusoidal in the *ac* plane. This porous structure enables compounds of appropriate size to enter and diffuse into the channels. In particular, silicalite is hydrophobic and organophilic, and hence it can adsorb organic molecules over water.

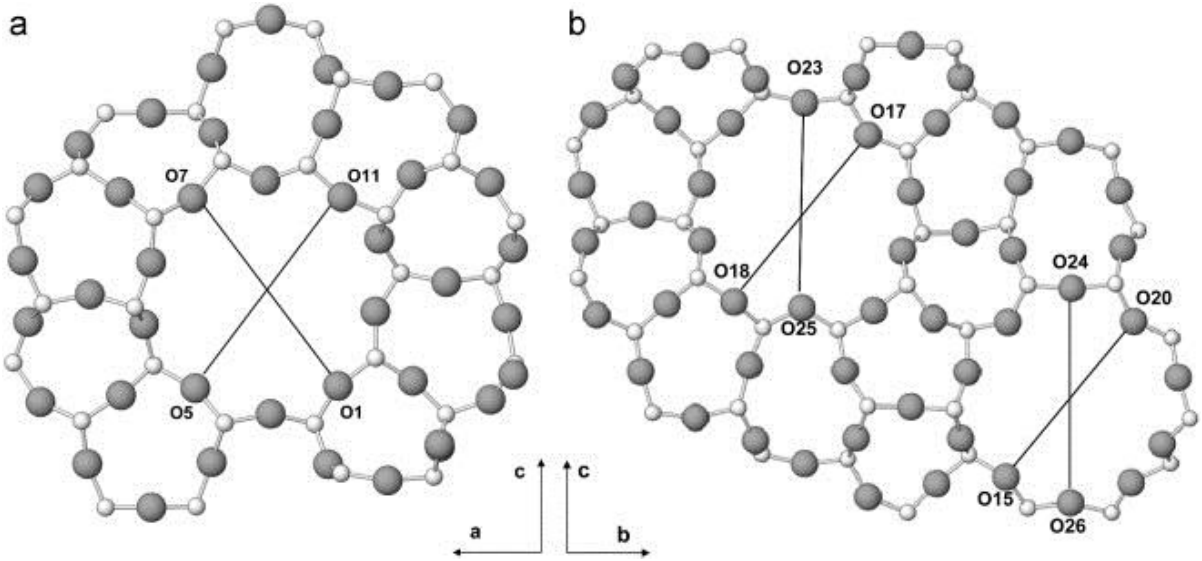

Fig. 1. (**a**) Projection of MFI-type structure along [0 1 0], showing the straight channels running parallel to the *b* axis; (**b**) (1 0 0) pentasil layer, showing the openings of the sinusoidal channels running along the *a* axis. The labeled atoms are used to measure the channel openings reported in Table 6 (gray balls: oxygen atoms, white balls: silicon atoms).

The maximum topological symmetry of MFI framework is orthorhombic (s.g. Pnma), but the real symmetry is strongly dependent on temperature, Si/Al ratio and extraframework content [6] and [7]. In particular, a reversible monoclinic ($P2_1/n$)/orthorhombic (Pnma) phase transition is induced in ZSM-5 and silicalite by

temperature, as a result of the relative shift of (0 1 0) pentasil layers in the *c* direction [8]. In silicalite this transition occurs at about 320 K, while the presence of aluminum in the framework lowers this temperature. For SiO_2/Al_2O_3<110 (i.e., Al>0.8 wt%), the transition occurs below room temperature [6] and hence the corresponding space group is Pnma already at ambient conditions.

Since the framework stability plays a crucial role in the processes involved in catalysis, like diffusion and adsorption, it is our aim to understand how it is influenced by another thermodynamic variable, i.e., pressure.

Recently, we have studied the elastic behavior of Na-ZSM-5 [9] and H-ZSM-5 [10] by synchrotron X-ray powder diffraction, using both (16:3:1) methanol:ethanol:water (m.e.w.) and silicone oil (s.o.), as "penetrating" and "non-penetrating" pressure transmitting media, respectively. Concerning the experiments in s.o., from P_{amb} to 6.2 GPa the observed volume reduction was 16.6 and 14.6% in H-ZSM-5 and Na-ZSM-5, respectively. The corresponding bulk moduli [K_0=23.7(4) GPa, K'=4 (fixed) and K_0=18.2(6) GPa, K'=4 (fixed)] testify that MFI-type materials are among the most flexible microporous materials up to now compressed in s.o. For both materials, the studies using m.e.w. revealed a strong increase in the extra-framework content, due to the penetration of additional water/alcohols molecules in the partially occupied extraframework sites. This penetration contributes to stiffen the structure and causes a higher bulk modulus with respect to the experiments in s.o.

The HP behavior of silicalite has been recently studied in s.o. by Haines et al. [11] and [12], in the frame of a project focused to study the pressure-induced amorphization (PIA) of this material. Two commercial silicalite samples (SOMEZ, France) were used: silicalite-1-OH [11] and silicalite-1-F, obtained by a fluoridric synthesis [12]. For the former sample, a phase transition from $P2_1/n$ to Pnma s.g. was observed at about 1 GPa and a bulk modulus of 18.8(5) GPa (K'=4) was determined. Moreover, PIA resulted to be strongly influenced by the incorporation of guest species (specifically CO_2 and Ar) inside silicalite pores, which tend to increase the amorphization pressure. The bulk modulus determined for silicalite-1-F was 13.6(5) GPa. The different compressibility values of the two materials was ascribed to non-equilibrium effects and to local depressurization due to the undergoing amorphization. No structural refinements of silicalite under HP are reported in these two papers.

In this work we discuss the compressibility behavior of mutinatite, the natural counterpart of MFI-type porous materials, and of two silicalite samples synthesized with different protocols (i.e., fluoridric and alkaline ambients), from now on labeled silicalite A and B, respectively.

The aims of the study are: (i) to follow in detail the structural modifications undergone by silicalite under HP; (ii) to compare the compressibility data of all the MFI-type materials up to now studied under HP and to interpret the different values on the basis of the zeolite framework and extra-framework composition.

2. Studied samples

2.1. Mutinaite

Mutinaite, $(Na_{2.76}K_{0.11}Mg_{0.21}Ca_{3.78})$ $(Al_{11.20}Si_{84.91}) \bullet 60H_2O$ [1] and [13], is orthorhombic, s.g. Pnma, with *a*=20.201(2), *b*=19.991(2), and *c*=13.469(2) Å. It was found in Ferrar dolerites at Mt. Adamson (Northern Victoria Land, Antarctica) associated with many other 5-ring zeolites like gottardiite, terranovaite, boggsite, tschernichite, heulandite, stilbite, stellerite, epistilbite, ferrierite, and mordenite. The Si/Al ratio of mutinaite (7.6) is the highest found to date in a natural zeolite, but it is by far the lowest among those of the synthetic zeolites with MFI-type framework, synthesized both in the presence and in the absence of any organic compound. The structure of mutinaite [13] is characterized by a strong disorder in the extraframework species: seventeen sites were detected in the channels, all with partial occupancies, low electron densities and at large distance from framework oxygens. For these reasons, no unambiguous identification of cations and water molecules was possible.

2.2. Silicalite A

Silicalite A was synthesized at Institut Charles Gerhardt de Montpellier using the bulk material dissolution technique, shown in Shimizu et al. [14], suitable to obtain millimetric crystals. Even if in this paper a powdered sample was used, that protocol was followed in order to obtain large silicalite crystals employed by our group in other single crystal studies. A piece of a glass tube (SiO_2=25.2 mmol) was placed in a PTFE sleeve equipped for an autoclave. The sleeve was filled with a reaction solution containing TPAOH as structure directing agent (8.9 mmol), hydrogen fluoride (HF=9.7 mmol) and water (H_2O=870 mmol). After the autoclave was heated at 200 °C for 25 day, the product crystals were washed with distilled water and dried at room temperature.

2.3. Silicalite B

Silicalite B was synthesized at Institut Charles Gerhardt de Montpellier using the following reagents: NaOH from Carlo Erba and tetrapropylammonium (TPA) bromide and tetraethyl orthosilicate (TEOS) from Aldrich. TEOS was added under stirring to the solution of NaOH and TPABr in deionized water to form a sol of composition 0.10 Na/0.11 TPA/SiO_2/100H_2O. The sol was aged 48 h at room temperature in a closed vessel, transferred into a stainless steel autoclave, sealed and heated at 50 °C for 6 day and at 130 °C for 48 h. The temperature-stepped synthesis procedure was based on literature reports [15] and [16].

3. Experimentals

3.1. Chemical and spectroscopic characterization of silicalite samples

Electron microprobe analyses of silicalite A and B were carried out at Padova University (IGG-CNR) using a Cameca SX 50 instrument in wavelength dispersive mode, equipped with a SAMx hardware-software system, operating at 20 kV and with a beam current of 2 nA and a spot beam (1 μm); counting times of 5, 10, and 5 s on high background, peak, and low background, respectively were used. The samples were prepared as pellets of 10 mg of powder by applying a pressure of 10 t/m^2. The standards used were albite Amelia for Al and Na, diopside for Si and Ca, orthoclase for K. Data acquisition and processing were performed using the XMAS program, based on the $\varphi(\rho z)$ data reduction (PAP). Water content was determined by thermogravimetric analysis on about 10 mg sample using a Seiko SSC/5200 instrument, operating at 5 °C/min from 20 to 900 °C in air. The total weight loss was 1.7 and 2.9% for silicalite A and B, respectively. Subtracting the contribution of the non-structural water (lost under 100 °C), the weight loss was 0.7 and 0.9%, respectively. The chemical data show that both silicalite A and B are virtually pure silica materials (Si/Al ratio equal to infinite), containing 2.5 and three water molecules in the formula unit, respectively.

3.2. X-ray powder diffraction experiments on silicalite samples at ambient conditions

The P_{amb} X-ray powder diffraction (XRPD) experiments on silicalite A and B were carried out with a diffractometer X'PERT PRO Panalytical with Bragg–Brentano geometry θ/θ and Cu K_α radiation. The samples were loaded in a zero background sample holder. The spectra were collected from 5 to 115° 2θ at a 400 s/° speed. Unit cell and structural parameters were determined by Rietveld profile fitting — using the GSAS package [17] with the EXPGUI [18] interface.

The starting atomic coordinates of the framework atoms were taken by [5], while the extraframework sites were located on the basis of the Fourier difference maps. The background curves were fitted by a Chebyshev polynomial with 18 coefficients. The pseudo-Voigt profile function proposed by Thomson et al. [19] and cut-off of the peak intensity were applied. In the first stages of the refinement soft-restraints were applied to the T–O distances [Si–O=1.61(2)] and the weight was gradually decreased down to a final value of 10. As an example of the data quality, the pattern collected on silicalite A and the corresponding calculated profile obtained after the refinement are reported in Fig. 2.

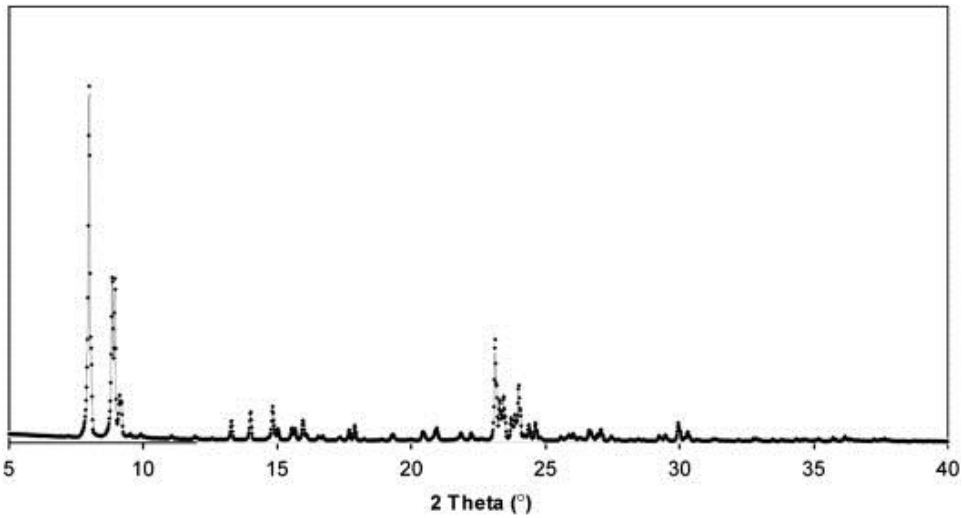

Fig. 2. Observed (diamonds) and calculated (continuous line) diffraction patterns from Rietveld refinement of silicalite A at P_{amb}.

3.3. Synchrotron X-ray powder diffraction experiments

The HP synchrotron XRPD experiments on mutinaite and silicalite B were performed at ID09 beamline (ESRF), while the data on silicalite A were collected at SNBL1 (BM01A) beamline (ESRF), using a modified Merril-Bassett DAC [20], and s.o. as *P*-transmitting medium. Table 1 reports selected experimental parameters relative to the three experiments. Pressure was calibrated using the ruby fluorescence method [21] on the non-linear hydrostatic pressure scale [22]. The estimated precision in the pressure values is 0.1 GPa. The samples were rocked to reduce texture in the diffraction images. For silicalite A and mutinaite some powder patterns were collected upon decompression, from the highest pressure to P_{amb}. The one-dimensional diffraction patterns were obtained by integrating the two dimensional images with the program FIT2D [23]. Selected integrated patterns are reported in Fig. 3(a)–(c) for mutinaite, silicalite A and silicalite B, respectively. Unit cell parameters were determined by Rietveld profile fitting — using the GSAS package [17] with the EXPGUI [18] interface. The isothermal bulk moduli of the three samples were determined with the EOS-FIT program [24], using a second-order Birch–Murnaghan equation of state [25].

Table 1. Experimental and structural refinement parameters for the XRPD measurements performed at ID09 and BM01A beamlines at ESRF.

	Mutinaite/Silicalite B (ID09 beamline, ESRF)	**Silicalite A (BM01A beamline, ESRF)**
λ	0.4132	0.70026
Detector	MAR345 (pixel dimension=150 μm)	MAR345 (pixel dimension=150 μm)
Sample-detector distance (mm)	365	221
Beam size (μm)	60	100
Exposure time (s)	20/5	180
P-range (GPa)	P_{amb}-6.0/P_{amb}-6.2	P_{amb}-6.6
Sample equilibration time (min)	15	30
Integration 2θ range of the powder patterns (°)	1.5–22	2.5–35

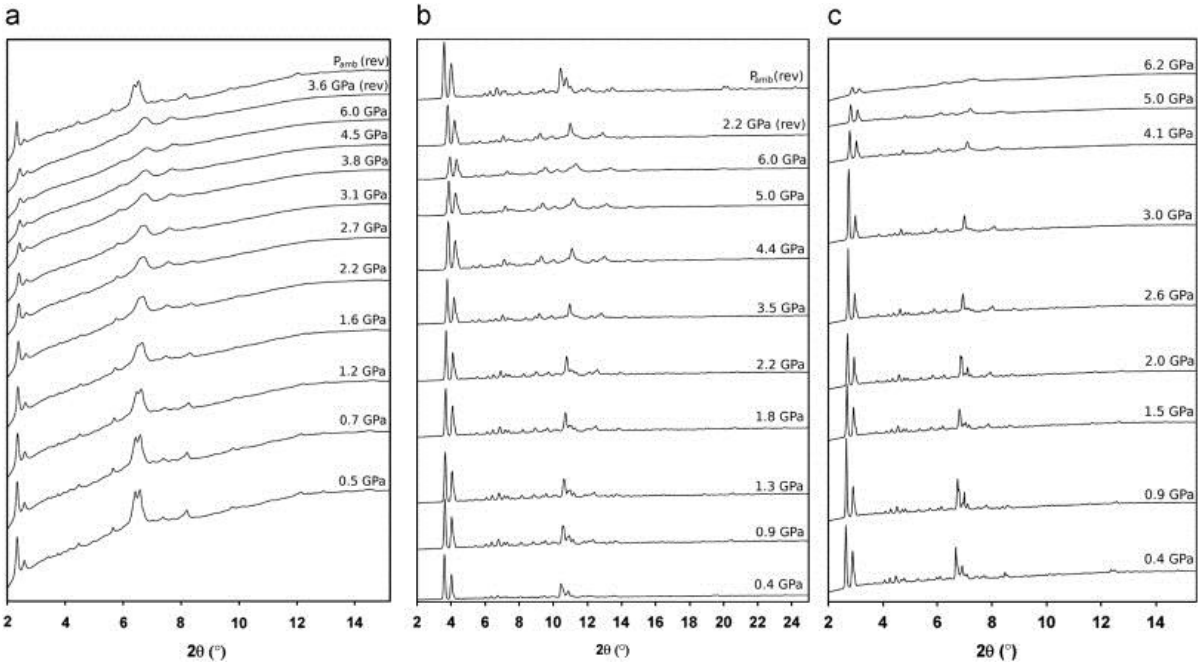

Fig. 3. Selected XRPD patterns as a function of pressure of (**a**) mutinaite, (**b**) silicalite A, and (**c**) silicalite B. The patterns at the top of the figures were collected during decompression.

3.3.1. Mutinaite

The unit cell parameters of mutinaite were determined up to 6 GPa. The Rietveld profile fitting of 10 patterns in the range 0.6–6.0 GPa and of three patterns collected at 5.0, 3.6 GPa and at P_{amb} upon pressure release were performed in the 2θ range 1.5–22. The starting atomic coordinates were taken by [13]. The refined cell parameters as a function of pressure are reported in Table 2 and Fig. 4(a). The quality of the powder data collected on mutinaite did not allow the complete structural refinements and the bulk modulus computation.

Table 2. Unit-cell parameters of mutinaite, silicalite A and silicalite B at the investigated pressures.

Mutinaite					
***P* (GPa)**	***a* (Å)**	***b* (Å)**	***c* (Å)**	***V* (Å^3)**	
P_{amb}	20.201(2)	19.991(2)	13.469(2)	5439.3(4)	
0.5	20.04(1)	19.73(1)	13.38(1)	5291(9)	
0.7	20.01(1)	19.68(1)	13.36(1)	5263(9)	
1.2	19.91(1)	19.55(1)	13.27(1)	5166(10)	
1.6	19.82(1)	19.43(1)	13.20(1)	5084(11)	
2.2	19.73(2)	19.33(2)	13.13(2)	5009(11)	
2.7	19.67(2)	19.25(2)	13.07(2)	4946(12)	
3.1	19.62(2)	19.19(2)	13.02(2)	4902(12)	
3.8	19.55(2)	19.11(2)	12.97(2)	4843(12)	
4.5	19.50(2)	19.05(2)	12.91(2)	4799(13)	
6.0	19.41(2)	18.94(2)	12.83(2)	4717(14)	
5.0 (rev)	19.45(2)	18.99(2)	12.85(2)	4747(14)	
3.6 (rev)	19.50(2)	19.08(2)	12.93(2)	4810(11)	
P_{amb} (rev)	20.16(1)	19.80(1)	13.49(2)	5384(10)	

Mutinaite					
***P* (GPa)**	***a* (Å)**	***b* (Å)**	***c* (Å)**	***V* (Å^3)**	
Silicalite A					
P (GPa)	*a*(Å)	*b*(Å)	*c*(Å)	*V*(Å^3)	*α*(°)
P_{amb}	20.1224(2)	19.8901(1)	13.3796(1)	5354.70(9)	90.631(1)
0.4	20.006(4)	19.801(4)	13.313(3)	5261(3)	90.54(2)
0.9	19.854(3)	19.679(3)	13.209(2)	5161(2)	
1.3	19.752(3)	19.587(3)	13.144(3)	5086(2)	
1.8	19.609(4)	19.466(4)	13.049(3)	4981(2)	
2.2	19.467(5)	19.334(5)	12.951(4)	4874(3)	
2.9	19.312(6)	19.177(7)	12.828(5)	4751(4)	
3.5	19.153(6)	19.005(7)	12.689(6)	4619(4)	
4.1	19.054(8)	18.856(9)	12.588(7)	4523(5)	
4.4	18.993(8)	18.779(9)	12.524(8)	4467(5)	
5.0	18.890(9)	18.65(1)	12.408(9)	4371(6)	
5.5	18.82(1)	18.57(1)	12.321(9)	4304(6)	
6.0	18.71(1)	18.45(1)	12.23(1)	4221(8)	
6.6	18.70(1)	18.42(2)	12.19(1)	4199(8)	
5.3 (rev)	18.64(1)	18.38(2)	12.15(1)	4162(8)	
2.2 (rev)	19.121(8)	18.950(9)	12.635(7)	4578(5)	
P_{amb} (rev)	20.140(4)	19.930(4)	13.426(3)	5389(3)	
Silicalite B					
P (GPa)	*a*(Å)	*b* (Å)	*c* (Å)	*V* (Å^3)	*α*(°)
P_{amb}	20.1268(3)	19.8933(4)	13.3855(3)	5359.1(2)	90.571(2)
0.4	20.062(2)	19.825(2)	13.328(2)	5300(1)	90.72(2)
1.0	19.860(4)	19.656(4)	13.200(3)	5153(2)	
1.5	19.669(3)	19.520(3)	13.086(2)	5024(2)	
2.0	19.490(4)	19.361(4)	12.954(3)	4888(2)	
2.6	19.308(4)	19.188(4)	12.819(3)	4749(2)	
3.0	19.160(5)	19.016(6)	12.699(4)	4627(3)	
3.5	18.975(5)	18.878(5)	12.606(4)	4521(3)	
4.1	18.853(6)	18.699(6)	12.496(5)	4405(3)	
4.6	18.701(7)	18.531(8)	12.383(6)	4291(4)	
5.0	18.601(8)	18.413(9)	12.311(7)	4217(5)	
5.5	18.434(7)	18.143(8)	12.111(4)	4050(2)	
6.2	18.349(8)	18.067(8)	12.062(5)	3999(2)	

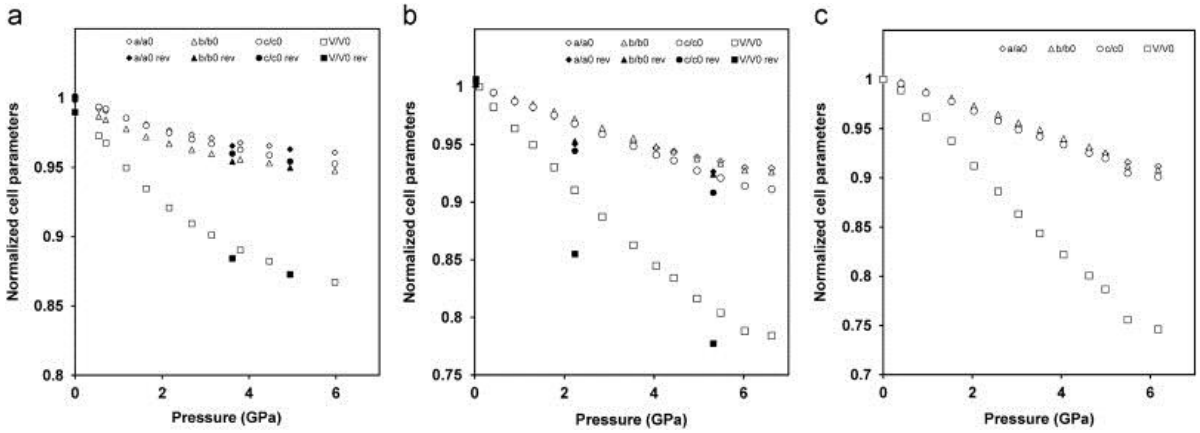

Fig. 4. Variation of (a) mutinaite, (b) silicalite A, and (c) silicalite B lattice parameters as a function of pressure. The errors associated with the cell parameters are smaller than the symbol size.

3.3.2. Silicalite A and B

The unit cell parameters of the two silicalite samples were determined by Rietveld profile fitting up to 6.6 GPa (15 patterns) and up to 6.2 GPa (13 patterns) for silicalite A and B, respectively. For silicalite A, three patterns were collected upon pressure release (at 5.3, 2.2 GPa and P_{amb}). The starting atomic coordinates were taken by [5]. The refined cell parameters as a function of pressure are reported in Table 2 and Fig. 4(b) and (c).

The quality of the powder data allowed the complete structural refinement of the patterns collected at P_{amb} for both samples, and at 0.9 GPa for silicalite A. The following structural refinement strategy was used: (i) the scale factor, the zero-shift, and the unit cell parameters were allowed to vary for all the refinement cycles; (ii) after the initial refinement cycles, the refined structural parameters for each data histogram were: fractional coordinates for all atoms (soft-restraints were applied to the TO distances [Si–O=1.60(2)–1.63(2)] and the weight was gradually decreased after the initial stages of refinement, down to a final weight of 10), occupancy factor for extraframework site and thermal isotropic displacement factors for all atoms (the isotropic displacement parameters were constrained in the following way: the same value for all tetrahedral cations, a second value for all framework oxygen atoms, and a third value for the extra-framework site); (iii) occupancy factor and isotropic thermal displacement factor for the extraframework site were varied in alternate cycles. The extraframework site was refined with the oxygen scattering curve.

Table 3 reports the details of the structural refinements at P_{amb} and 0.9 GPa of silicalite A, which will be discussed below. The results of the refinements (atomic coordinates, thermal parameters and bond distances) are reported in Table 4(a), (b) and Table 5.

Table 3. Details of the structural refinements of silicalite A at P_{amb} and 0.9 GPa.

	P_{amb}	0.9 GPa
R_p	0.07	0.01
Rw_p	0.10	0.01
R_F^2	0.08	0.12
No. of variables	244	144
No. of observations	14,835	1180

Table 4. (a) – Refined atomic positions, occupancy factors and displacement parameters (Å^2) of silicalite A at P_{amb}.

	x/a	y/b	z/c	Occ	Uiso
Si1	0.421(2)	0.056(2)	−0.320(2)	1	0.033(2)
Si2	0.313(2)	0.031(1)	−0.168(2)	1	0.033(2)
Si3	0.283(2)	0.057(1)	0.034(2)	1	0.033(2)
Si4	0.127(2)	0.057(2)	0.043(2)	1	0.033(2)
Si5	0.070(2)	0.034(2)	−0.177(2)	1	0.033(2)
Si6	0.202(2)	0.061(2)	−0.302(2)	1	0.033(2)
Si7	0.426(2)	−0.167(2)	−0.325(2)	1	0.033(2)
Si8	0.311(2)	−0.124(1)	−0.176(2)	1	0.033(2)
Si9	0.271(2)	−0.173(2)	0.042(2)	1	0.033(2)
Si10	0.118(2)	−0.183(2)	0.040(2)	1	0.033(2)
Si11	0.070(2)	−0.128(1)	−0.171(2)	1	0.033(2)
Si12	0.189(2)	−0.165(2)	−0.317(2)	1	0.033(2)
Si13	0.426(1)	0.446(2)	−0.334(2)	1	0.033(2)
Si14	0.312(2)	0.474(1)	−0.191(2)	1	0.033(2)
Si15	0.279(2)	0.447(1)	0.037(2)	1	0.033(2)
Si16	0.124(2)	0.439(2)	0.028(2)	1	0.033(2)
Si17	0.078(2)	0.472(1)	−0.195(2)	1	0.033(2)
Si18	0.186(2)	0.436(1)	−0.320(2)	1	0.033(2)
Si19	0.418(2)	0.671(2)	−0.331(2)	1	0.033(2)
Si20	0.315(2)	0.633(1)	−0.164(2)	1	0.033(2)
Si21	0.273(2)	0.670(2)	0.052(2)	1	0.033(2)
Si22	0.119(2)	0.678(2)	0.045(2)	1	0.033(2)
Si23	0.081(2)	0.632(2)	−0.179(2)	1	0.033(2)
Si24	0.197(2)	0.675(1)	−0.306(2)	1	0.033(2)
O1	0.377(3)	0.063(3)	−0.219(4)	1	0.036(2)
O2	0.330(2)	0.063(3)	−0.061(3)	1	0.036(2)
O3	0.205(2)	0.049(3)	0.024(4)	1	0.036(2)
O4	0.103(3)	0.058(3)	−0.072(3)	1	0.036(2)
O5	0.128(2)	0.046(3)	−0.258(4)	1	0.036(2)
O6	0.246(2)	0.066(3)	−0.201(3)	1	0.036(2)
O7	0.380(2)	−0.153(3)	−0.225(4)	1	0.036(2)
O8	0.301(4)	−0.160(3)	−0.068(3)	1	0.036(2)
O9	0.193(2)	−0.158(3)	0.042(3)	1	0.036(2)
O10	0.092(3)	−0.170(3)	−0.073(3)	1	0.036(2)
O11	0.119(2)	−0.149(3)	−0.260(3)	1	0.036(2)
O12	0.245(2)	−0.133(3)	−0.242(4)	1	0.036(2)
O13	0.320(3)	−0.046(1)	−0.149(4)	1	0.036(2)
O14	0.081(3)	−0.047(1)	−0.171(4)	1	0.036(2)
O15	0.417(3)	0.123(2)	−0.386(4)	1	0.036(2)
O16	0.394(3)	−0.001(2)	−0.394(4)	1	0.036(2)
O17	0.401(3)	−0.132(2)	−0.427(4)	1	0.036(2)
O18	0.191(3)	0.130(2)	−0.363(3)	1	0.036(2)

	x/a	y/b	z/c	Occ	Uiso
O19	0.197(3)	0.001(2)	−0.383(3)	1	0.036(2)
O20	0.206(4)	−0.127(2)	−0.421(3)	1	0.036(2)
O21	−0.001(1)	0.061(3)	−0.215(4)	1	0.036(2)
O22	−0.008(2)	−0.145(3)	−0.194(4)	1	0.036(2)
O23	0.423(3)	−0.248(2)	−0.339(4)	1	0.036(2)
O24	0.203(3)	−0.246(2)	−0.333(3)	1	0.036(2)
O25	0.287(3)	−0.250(2)	−0.068(4)	1	0.036(2)
O26	0.104(3)	−0.251(2)	0.099(3)	1	0.036(2)
O27	0.376(2)	0.437(3)	−0.240(4)	1	0.036(2)
O28	0.306(4)	0.453(3)	−0.076(3)	1	0.036(2)
O29	0.203(2)	0.433(3)	−0.004(4)	1	0.036(2)
O30	0.090(3)	0.450(3)	−0.081(3)	1	0.036(2)
O31	0.116(2)	0.421(2)	−0.267(4)	1	0.036(2)
O32	0.253(2)	0.442(3)	−0.255(4)	1	0.036(2)
O33	0.379(3)	0.643(3)	−0.235(4)	1	0.036(2)
O34	0.316(3)	0.653(3)	−0.046(2)	1	0.036(2)
O35	0.196(2)	0.656(2)	0.029(4)	1	0.036(2)
O36	0.094(3)	0.652(3)	−0.062(3)	1	0.036(2)
O37	0.121(2)	0.663(3)	−0.269(4)	1	0.036(2)
O38	0.253(3)	0.663(3)	−0.222(4)	1	0.036(2)
O39	0.301(4)	0.555(1)	−0.188(4)	1	0.036(2)
O40	0.083(3)	0.552(1)	−0.207(4)	1	0.036(2)
O41	0.411(3)	0.383(2)	−0.406(4)	1	0.036(2)
O42	0.419(3)	0.495(2)	−0.426(3)	1	0.036(2)
O43	0.395(3)	0.633(2)	−0.433(3)	1	0.036(2)
O44	0.185(2)	0.363(2)	−0.375(3)	1	0.036(2)
O45	0.207(3)	0.500(2)	−0.385(3)	1	0.036(2)
O46	0.207(4)	0.617(2)	−0.390(3)	1	0.036(2)
O47	−0.001(2)	0.456(3)	−0.207(4)	1	0.036(2)
O48	0.001(2)	0.644(3)	−0.190(4)	1	0.036(2)
W1	0.242(2)	0.730(3)	0.384(4)	0.76(3)	0.15(4)

(b) Refined atomic positions, occupancy factors and displacement parameters (Å^2) *of silicalite A at* 0.9 GPa.

	x/a	y/b	z/c	Occ	Uiso
Si1	0.432(2)	0.047(3)	−0.340(3)	1	0.034(3)
Si2	0.333(2)	0.025(2)	−0.164(4)	1	0.034(3)
Si3	0.276(2)	0.043(2)	0.043(4)	1	0.034(3)
Si4	0.121(2)	0.072(2)	0.023(4)	1	0.034(3)
Si5	0.083(2)	0.026(2)	−0.198(4)	1	0.034(3)
Si6	0.215(2)	0.075(3)	−0.298(2)	1	0.034(3)
Si7	0.424(3)	−0.170(1)	−0.323(4)	1	0.034(3)
Si8	0.306(3)	−0.133(2)	−0.179(4)	1	0.034(3)
Si9	0.273(2)	−0.170(1)	0.041(4)	1	0.034(3)
Si10	0.115(2)	−0.175(2)	0.034(4)	1	0.034(3)

	x/a	y/b	z/c	Occ	Uiso
Si11	0.074(2)	−0.133(2)	−0.190(3)	1	0.034(3)
Si12	0.195(2)	−0.173(2)	−0.333(3)	1	0.034(3)
O1	0.379(4)	0.056(5)	−0.251(5)	1	0.037(4)
O2	0.331(3)	0.034(2)	−0.044(4)	1	0.037(4)
O3	0.201(3)	0.070(4)	0.037(5)	1	0.037(4)
O4	0.097(4)	0.060(5)	−0.090(3)	1	0.037(4)
O5	0.145(2)	0.069(4)	−0.240(4)	1	0.037(4)
O6	0.274(3)	0.066(4)	−0.218(4)	1	0.037(4)
O7	0.376(2)	−0.148(5)	−0.232(5)	1	0.037(4)
O8	0.308(4)	−0.164(3)	−0.067(4)	1	0.037(4)
O9	0.193(2)	−0.173(2)	0.057(5)	1	0.037(4)
O10	0.091(4)	−0.157(5)	−0.078(3)	1	0.037(4)
O11	0.135(3)	−0.144(4)	−0.267(5)	1	0.037(4)
O12	0.242(3)	−0.161(4)	−0.238(5)	1	0.037(4)
O13	0.313(4)	−0.053(2)	−0.179(5)	1	0.037(4)
O14	0.079(3)	−0.053(2)	−0.215(6)	1	0.037(4)
O15	0.410(5)	0.106(3)	−0.416(6)	1	0.037(4)
O16	0.402(4)	−0.006(3)	−0.419(7)	1	0.037(4)
O17	0.409(4)	−0.141(3)	−0.433(5)	1	0.037(4)
O18	0.194(3)	0.142(2)	−0.357(4)	1	0.037(4)
O19	0.221(4)	0.026(2)	−0.394(5)	1	0.037(4)
O20	0.193(4)	−0.110(3)	−0.409(5)	1	0.037(4)
O21	0.007(2)	0.053(5)	−0.202(6)	1	0.037(4)
O22	0.0004(30)	−0.161(5)	−0.212(5)	1	0.037(4)
O23	0.439(5)	−0.25	−0.329(9)	1	0.037(4)
O24	0.185(7)	−0.25	−0.368(6)	1	0.037(4)
O25	0.285(6)	−0.25	0.040(9)	1	0.037(4)
O26	0.115(4)	−0.25	0.079(6)	1	0.037(4)
W1	0.382(4)	0.25	0.925(6)	0.87(4)	0.015

Table 5. T–O framework distances (Å) for silicalite A at P_{amb} and 0.9 GPa.

		P_{amb}			**0.9 GPa**
Si1-	**O1**	1.62(2)	**Si1-**	O1	1.592(5)
	O15	1.62(2)		O15	1.590(5)
	O15	1.59(2)		O16	1.591(5)
	O47	1.63(2)		O21	1.592(5)
Mean		1.62			1.591
Si2-	**O1**	1.61(2)	**Si2-**	**O1**	1.592(5)
	O2	1.60(2)		**O2**	1.594(5)
	O6	1.58(2)		**O6**	1.592(5)
	O13	1.56(2)		**O13**	1.592(5)
Mean		1.59			1.592

		P_{amb}			0.9 GPa
Si3-	**O2**	1.59(2)	**Si3-**	**O2**	1.592(5)
	O3	1.58(2)		**O3**	1.594(5)
	O45	1.58(2)		**O19**	1.591(5)
	O46	1.58(2)		**O20**	1.591(5)
Mean		1.58			1.592
Si4-	**O3**	1.60(2)	**Si4-**	**O3**	1.594(5)
	O4	1.61(2)		**O4**	1.594(5)
	O42	1.60(2)		**O16**	1.592(5)
	O43	1.61(2)		**O17**	1.591(5)
Mean		1.61			1.592
Si5-	**O4**	1.62(2)	**Si5-**	**O4**	1.593(5)
	O5	1.61(2)		**O5**	1.591(5)
	O14	1.62(2)		**O14**	1.592(5)
	O21	1.61(2)		**O21**	1.591(5)
Mean		1.62			1.592
Si6-	**O5**	1.63(2)	**Si6-**	**O5**	1.592(5)
	O6	1.61(2)		**O6**	1.592(5)
	O18	1.62(2)		**O18**	1.592(5)
	O19	1.60(2)		**O19**	1.593(5)
Mean		1.62			1.592
Si7-	**O7**	1.64(2)	**Si7-**	**O7**	1.593(5)
	O17	1.62(2)		**O17**	1.591(5)
	O23	1.63(2)		**O22**	1.591(5)
	O48	1.60(2)		**O23**	1.590(5)
Mean		1.62			1.591
Si8-	**O7**	1.65(2)	**Si8-**	**O7**	1.593(5)
	O8	1.63(2)		**O8**	1.592(5)
	O12	1.60(2)		**O12**	1.591(5)
	O13	1.59(2)		**O13**	1.591(5)
Mean		1.62			1.591
Si9-	**O8**	1.62(2)	**Si9-**	**O8**	1.593(5)
	O9	1.58(2)		**O9**	1.592(5)
	O25	1.61(2)		**O25**	1.591(5)
	O44	1.60(2)		**O18**	1.591(5)
Mean		1.60			1.591
Si10-	**O9**	1.60(2)	**Si10-**	**O9**	1.591(5)
	O10	1.61(2)		**O10**	1.594(5)
	O26	1.60(2)		**O26**	1.591(5)
	O41	1.59(2)		**O15**	1.590(5)
Mean		1.60			1.591
Si11-	**O10**	1.63(2)	**Si11-**	**O10**	1.594(5)

		P_{amb}			0.9 GPa
	O11	1.61(2)		**O11**	1.589(5)
	O12	1.62(2)		**O14**	1.592(5)
	O22	1.63(2)		**O22**	1.592(5)
Mean		1.62			1.592
Si12-	**O11**	1.63(2)	**Si12-**	**O11**	1.591(5)
	O12	1.62(2)		**O12**	1.592(5)
	O20	1.62(2)		**O20**	1.592(5)
	O24	1.64(2)		**O24**	1.593(5)
Mean		1.63			1.592
Si13-	**O21**	1.61(2)			
	O27	1.62(2)			
	O41	1.60(2)			
	O42	1.59(2)			
Mean		1.61			
Si14-	**O27**	1.62(2)			
	O28	1.60(2)			
	O32	1.59(2)			
	O39	1.62(2)			
Mean		1.61			
Si15-	**O19**	1.58(2)			
	O20	1.61(2)			
	O28	1.62(2)			
	O29	1.61(2)			
Mean		1.61			
Si16-	**O16**	1.62(2)			
	O17	1.62(2)			
	O29	1.63(2)			
	O30	1.63(2)			
Mean		1.63			
Si17-	**O30**	1.61(2)			
	O31	1.58(2)			
	O40	1.59(2)			
	O47	1.61(2)			
Mean		1.60			
Si18-	**O31**	1.61(2)			
	O32	1.61(2)			
	O44	1.63(2)			
	O45	1.61(2)			
Mean		1.62			
Si19-	**O22**	1.61(2)			
	O23	1.63(2)			

		P_{amb}			0.9 GPa
	O33	1.61(2)			
	O43	1.62(2)			
Mean		1.62			
Si20-	**O33**	1.61(2)			
	O34	1.62(2)			
	O38	1.60(2)			
	O39	1.62(2)			
Mean		1.61			
Si21-	**O18**	1.58(2)			
	O25	1.61(2)			
	O34	1.60(2)			
	O35	1.60(2)			
Mean		1.60			
Si22-	**O15**	1.60(2)			
	O26	1.62(2)			
	O35	1.62(2)			
	O36	1.60(2)			
Mean		1.61			
Si23-	**O36**	1.63(2)			
	O37	1.60(2)			
	O40	1.63(2)			
	O48	1.62(2)			
Mean		1.62			
Si24-	**O24**	1.63(2)			
	O37	1.61(2)			
	O38	1.61(2)			
	O46	1.61(2)			
Mean		1.62			

4. Results and discussion

4.1. Elastic behavior

Fig. 3(a)–(c) – reporting selected powder patterns of mutinaite, silicalite A and silicalite B – shows that the peak intensities decrease and the peak profiles become broader with increasing pressure. Moreover, the features present in the patterns collected at low pressure are only partially regained upon decompression from HP.

While in mutinaite no symmetry change is observed as a function of P, a phase transition from monoclinic ($P2_1/n$) to orthorhombic (Pnma) symmetry is observed at about 1.0 GPa in both silicalite samples. The phase transition — which strictly corresponds to that found at 1.1 GPa by Haines et al. [11] — is particularly evident for silicalite B in the 6.1–6.7 and 7.7–8.2 spectral 2θ regions (Fig. 5). It is worth noting that, on the

basis of the unit cell parameters reported in Table 2 and from the inspection of the powder patterns, this phase transition results to be not reversible upon decompression.

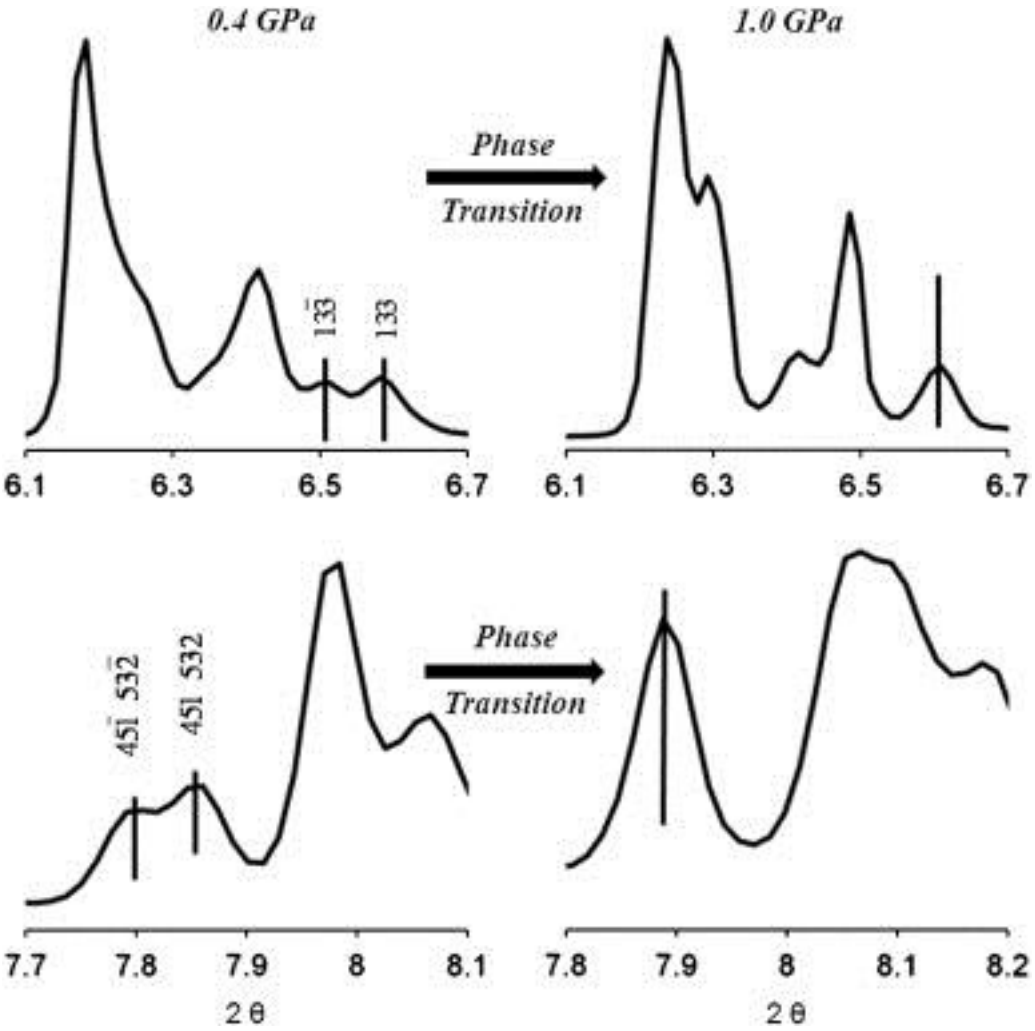

Fig. 5. Selected 2θ ranges of X-ray powder patterns of the silicalite B at 0.4 and 1.0 GPa showing the change of symmetry.

Compressibility of mutinaite is rather isotropic, with the following unit cell parameter decreases: 3.9, 5.2, 4.7 and 13.2% for *a*, *b*, *c* and *V*, respectively (Fig. 4(a) and Table 2). Contrary to peak intensities, the original unit cell parameters are rather well recovered upon decompression (Fig. 3(a) and Table 2).

Concerning silicalite samples, the elastic behavior is similar for the two phases, with an almost isotropic cell axes contraction, especially at low pressure (Fig. 4(b), (c) and Table 2). In particular, the cell parameter decreases are 7.0, 7.4, 8.9 and 21.6% for *a*, *b*, *c*, and *V* for silicalite A and 8.8, 9.2, 9.9 and 25.4% for silicalite B, respectively. The elastic parameters were calculated after the fulfillment of the phase transition (from 1.3 and from 1.0 GPa for silicalite A and B, respectively). The second order (K'=4 fixed) bulk moduli obtained using the data weighted by the uncertainties in *P* and *V*, are K_0=18.2(2) and K_0=14.3 (2) GPa for silicalite A and silicalite B, respectively. Since the bulk modulus values determined for zeolites compressed in ‘‘non-penetrating’’ media range from about 18–72 GPa [26], silicalite can be classified as the most compressible zeolite up to now studied under these conditions.

The different compressibility of the two silicalite samples – which are comparable from the chemical and structural point of view – can be interpreted with the help of the IR data collected on the degased powders [27]. The spectroscopic results (Fig. 6), showing the typical band of the O–H stretching at about 3600 cm^{-1}, clearly indicate that silicalite B (synthesized in alkaline ambient) contains a significantly higher amount of hydroxyls with respect to silicalite A (synthesized in fluoridric ambient). These structural defects certainly

influence the zeolite HP behavior, increasing silicalite B compressibility. Actually, our results are in some disagreement with those reported by Haines et al. [11] and [12]: these authors determined a higher K_0 value for silicalite-1-OH (18.8(5) GPa) [11] than for silicalite-1-F (13.6(5) GPa) [12]. However, this apparent incongruence could be due, as also observed by the same authors [11], by non-equilibrium effects during compression.

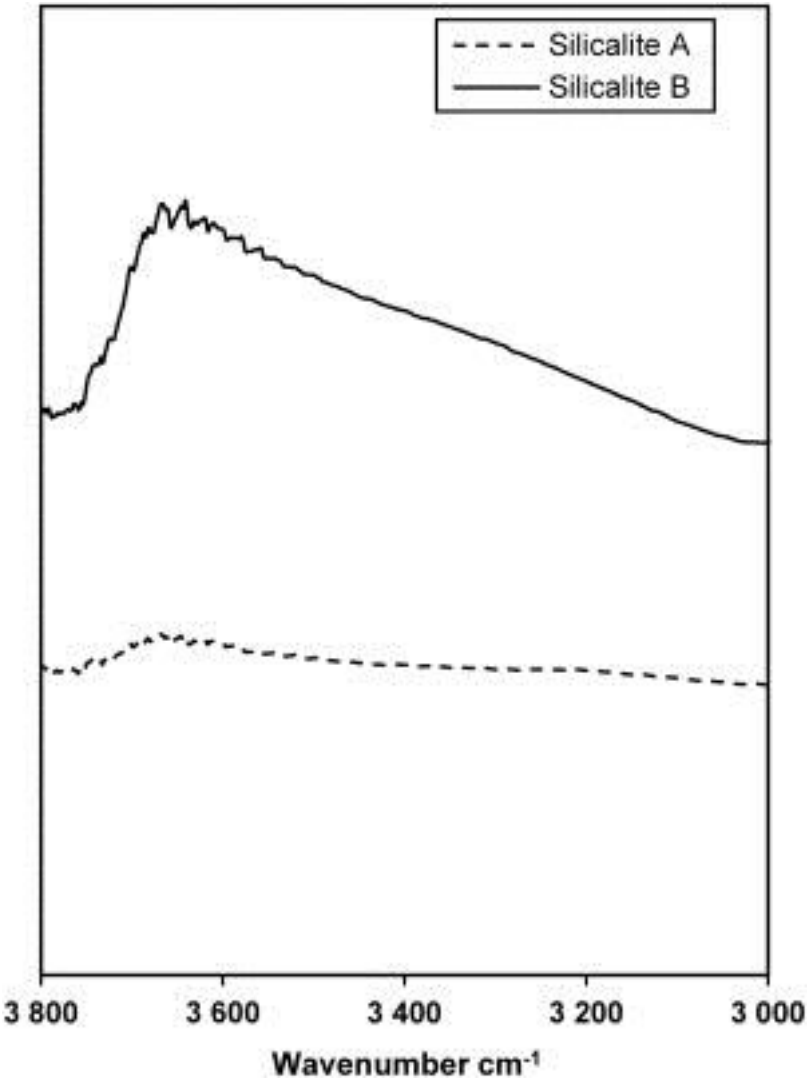

Fig. 6. IR spectra of degassed silicalite A and B samples, showing the typical band of the O–H stretching at about 3600 cm^{-1}.

4.2. Structural interpretation of the HP-induced phase transition in silicalite

The structural deformations induced by HP in silicalite A were investigated by means of complete Rietveld structural refinements, before and after the phase transition from $P2_1/n$ to Pnma s.g. (at P_{amb} and 0.9 GPa, respectively). The analogous phase transition observed in silicalite B was not studied in detail due to the lower data quality. Above 0.9 GPa, the powder pattern quality of both samples and the high number of structural parameters made it impossible to obtain reliable structural data on the more compressed materials. Fig. 7 shows the projections of silicalite A structure before and after the phase transition, evidencing the framework and extraframework modifications related to the symmetry change.

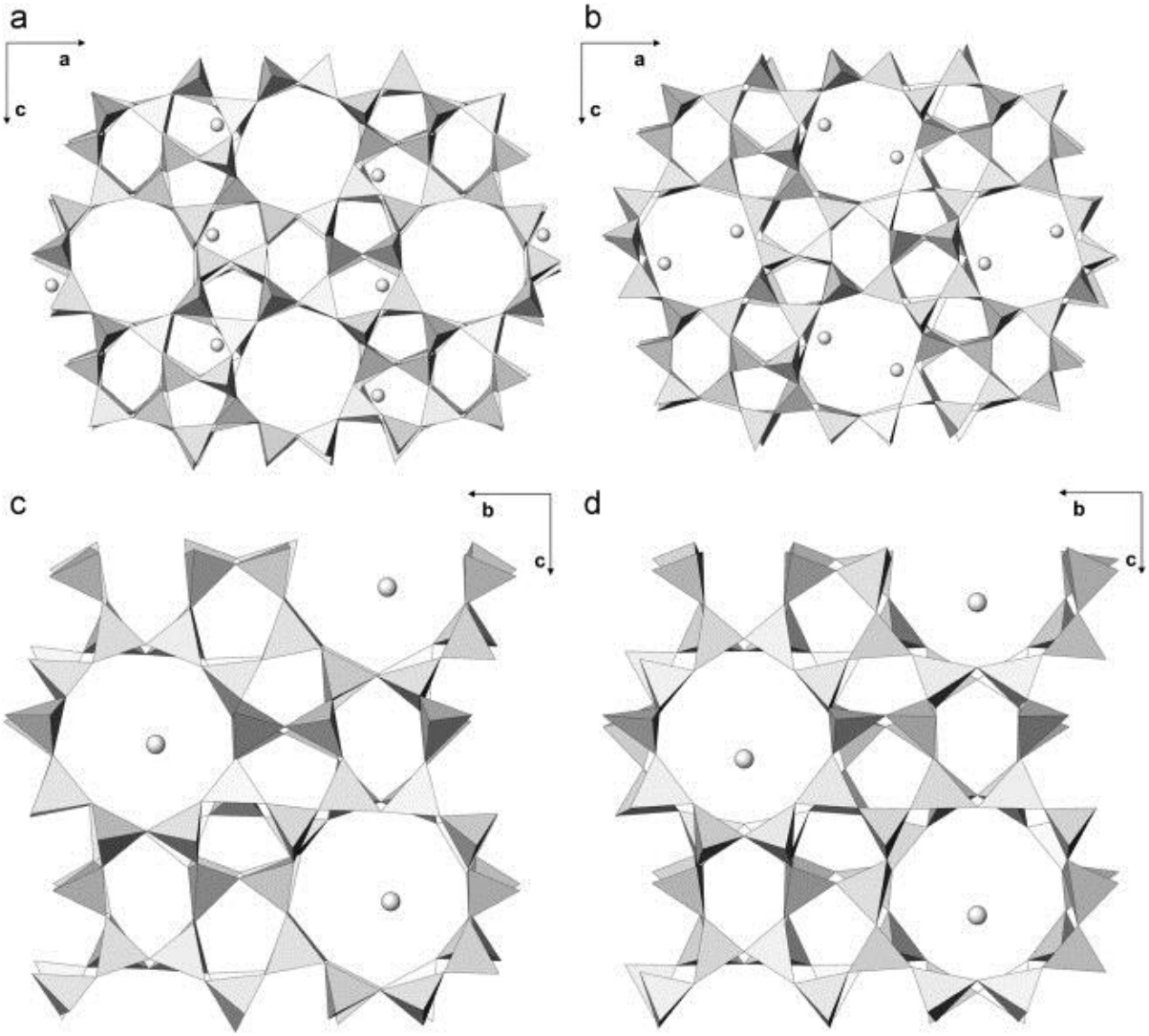

Fig. 7. Projection of the silicalite A structure along the direction of the straight [0 1 0] (a) and (b) and sinusoidal [1 0 0] (c) and (d) channels at *P*amb (a) and (c) and 0.9 GPa (b) and (d), respectively.

At ambient conditions, silicalite A is monoclinic s.g. $P2_1/n$ (Table 4). Only one extraframework site, partially occupied by water molecules, has been located. As a whole, about three water molecules were found by the structure refinement (in excellent agreement with the thermogravimetric analysis results). The most evident HP-induced modifications involve the position of this water site, which moves toward the center of the straight channel (Fig. 7(b)). Fig. 7(d) shows that, in the orthorhombic symmetry, the water site is placed on the mirror plane perpendicular to the *b* axis.

Concerning the framework response to pressure, Table 6 reports the window openings and the ellipticity indices of the straight and sinusoidal 10-ring channels at P_{amb} and 0.9 GPa. The channel ellipticity was calculated as in [10] on the basis of the following distances ratios: (O1–O7)/(O5–O11) for the straight channel, and (O15–O20)/(O24–O26), and (O17–O18)/(O23–O25) for the sinusoidal ones (Fig. 1). The values of the [0 1 0] straight channel ellipticity calculated at P_{amb} and 0.9 GPa (0.98 and 0.94, respectively), indicate that the shape of the straight channel opening is only slightly affected by compression. Actually, notwithstanding the ellipticity remains almost constant with increasing pressure, we observe an increase of both the diagonal distances of this channel (O1–O7 and O5–O11 in Table 6), accompanied by a visible distortion of the 5-membered rings (Fig. 7(a) and (b)). On the other hand, the shape of the sinusoidal [1 0 0] channel is more affected by compression, becoming more elliptic at 0.9 GPa (Table 6 and Fig. 7(c) and (d)).

Table 6. Window openings (Å) and ellipticity of the straight and sinusoidal 10-ring channels of silicalite A at P_{amb} and 0.9 GPa. Atom labels are from the orthorhombic structure and refer to Fig. 1.

	Straight channel along [0 1 0]		
***P*(GPa)**	**O5–O11**	**O1–O7**	**(O1–O7)/(O5–O11)**
P_{amb}	8.00	7.87	0.98
0.9	8.69	8.22	0.94

	Sinusoidal channels along [1 0 0]					
***P*(GPa)**	**O15–O20**	**O24–O26**	**O23–O25**	**O17–O18**	**(O15–O20)/(O24–O26)**	**(O17–O18)/(O23–O25)**
P_{amb}	8.29	7.26	8.39	7.69	1.05	0.92
0.9	8.95	7.44	8.87	7.34	0.83	1.20

5. Comparative discussion of the High-pressure behavior of MFI-type Phases

It is interesting to compare the elastic behavior of mutinaite and silicalite compressed in non-penetrating *P*-transmitting medium with that of Na-ZSM-5 [9] and H-ZSM-5 [10], the other MFI-type zeolites recently studied by our group under the same experimental conditions. Since these materials have the same framework topology, but different framework and extraframework compositions, we have the unique opportunity to compare their compressibility in the same pressure range (see Fig. 8) and to interpret it on the structural and chemical basis. Table 7 reports the HP-induced unit cell parameter reductions for the five materials, together with Si/Al ratio, number of water molecules derived by the chemical analysis, and total extraframework content (expressed as the total number of electrons of the cations and water molecules) derived from the refinement.

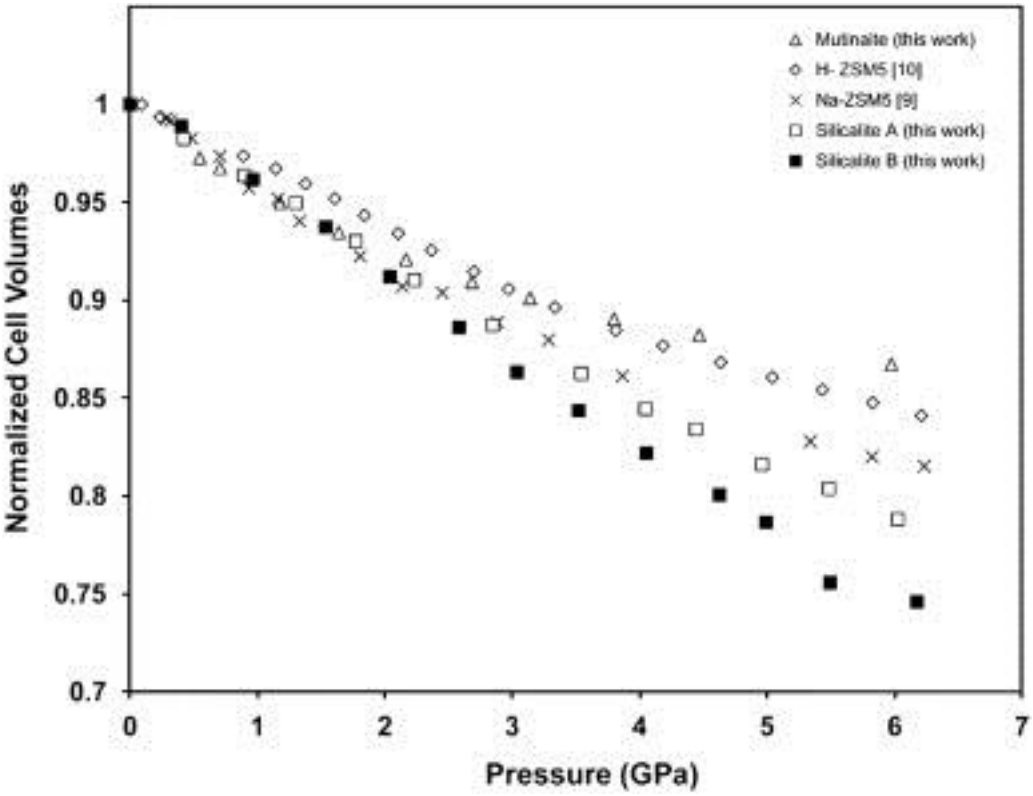

Fig. 8. Comparison of the unit-cell volume variations as a function of pressure for mutinaite, H-ZSM5, Na-ZSM5, silicalite A, and silicalite B compressed in silicone oil.

Table 7. Unit cell parameters variations of the MFI-type zeolites studied in s.o. in the pressure range P_{amb}–6 GPa. The chemical composition of the five phases is expressed as Si/Al ratio (EMPA analyses), number of water molecules (TG analyses), and total number of extraframework electrons (structural refinements).

Sample	Δ*a* (%)	Δ*b* (%)	Δ*c* (%)	Δ*V* (%)	Si/Al ratio	No. of water molecules	No. of extra-framework electrons
Mutinaite (up to 6.0 GPa)	3.9	5.2	4.7	13.2	7.6	60.0	711
H-ZSM-5 (up to 6.2 GPa)[10]	5.9	6.0	5.7	16.6	11.4	36.0	379
Na-ZSM-5 (up to 6.2 GPa)[9]	6.4	6.3	6.9	18.5	18.3	28.4	343
Silicalite A (up to 6.0 GPa)	7.0	7.2	8.6	21.2	∞	2.5	24 (=3 water molecules)
Silicalite B (up to 6.2 GPa)	8.8	9.2	9.9	25.4	∞	3.0	25 (=3 water molecules)

It is evident that the phases with the lowest Si/Al ratios, and as a consequence the highest extraframework contents, show the lowest cell parameter contractions. In fact, the most compressible phases are the two silicalite samples, which are characterized by almost empty pores. In particular, the higher contractions of silicalite B with respect to silicalite A are favored by the presence of a significant amount of hydroxyl defects. On the contrary, the most rigid material is mutinaite, which is characterized by the presence of a high number of cation and water sites [13] in the channels. We can hence conclude that the response of MFI-type materials to pressure is strongly dependent on the extra-framework species, which contribute to stiffen the structure and to contrast the HP-induced channel deformations. These results are in agreement with the conclusions of other HP studies performed with non-penetrating P-transmitting media on zeolites [28], [29], [30] and [31] and are particularly highlighted by the studies on zeolites with chabazite topology [26] and [32] and on fibrous zeolites [33].

Acknowledgments

BM01 and ID09 beamlines at European Synchrotron Radiation Facility are acknowledged for allocation of the experimental beamtime. The authors are indebted with Marco Merlini for the assistance during the diffraction experiments at ID09. Two anonymous reviewers and the Editor-in-Chief Mercouri G. Kanatzidis improved the quality of the manuscript. Dr. Simona Bigi and Dr. Raul Carampin are acknowledged for the EMPA and TG analyses. This work was supported by the Italian MIUR (PRIN2008).

References

[1] E. Galli, G. Vezzalini, S. Quartieri, A. Alberti, M. Franzini
Zeolites, 18 (1997), pp. 318–322

[2] G.T. Kokotailo, S.L. Lawton, O.H. Olson, W.M. Meier
Nature, 272 (1978), pp. 437–438

[3] D.H. Olson, G.T. Kokotailo, S.L. Lawton, W.M. Meier
J. Phys. Chem., 85 (1981), pp. 2238–2243

[4] E.M. Flaningen, J.M. Bennett, R.W. Grose, J.P. Cohen, R.L. Patton, R.M. Kirchner, J.V. Smith
Nature, 271 (1978), pp. 512–516

[5] G. Artioli, C. Lamberti, G.L. Marra
Acta Crystallogr., Sect. B, 56 (2000), pp. 2–10

[6] D.G. Hay, H. Jaeger
J. Chem. Soc., Chem. Commun. (1984), p. 1433

[7] E. de Vos Burchart, H. van Bekkum, B. van de Graaf
Zeolites, 13 (1993), pp. 212–215

[8] H. van Koningsveld, J.C. Jansen, H. van Bekkum
Zeolites, 7 (1987), pp. 564–568

[9] R. Arletti, G. Vezzalini, A. Morsli, F. Di Renzo, V. Dmitriev, S. Quartieri
Microporous Mesoporous Mater., 142 (2011), pp. 696–707

[10] S. Quartieri, G. Montagna, R. Arletti, G. Vezzalini
J. Sol. St. Chem., 184 (2011), pp. 1505–1516

[11] J. Haines, O. Cambon, C. Levelut, M. Santoro, F. Gorelli, G. Garbarino
J. Am. Chem. Soc., 132 (2010), pp. 8860–8861

[12] J. Haines, C. Levelut, A. Isambert, Ph. Hebert, S. Kohara, D.A. Keen, T. Hammouda, D. Andrault
J. Am. Chem. Soc., 131 (2009), pp. 12333–12338

[13] G. Vezzalini, S. Quartieri, E. Galli, A. Alberti, G. Cruciani, Å. Kvick
Zeolites, 19 (1997), pp. 323–325

[14] S. Shimizu, H. Hamada
Microporous Mesoporous Mater., 48 (2001), pp. 39–46

[15] Q. Li, D. Creaser, J. Sterte
Microporous Mesoporous Mater., 31 (1999), pp. 141–150

[16] C.S. Cundy
Zeolites and ordered Mesoporous materials: progress and prospects
J. Čejka, H. van Bekkum (Eds.), Studies in Surface Science and Catalysis, 157, Elsevier Science B.V, Amsterdam (2005), pp. 65–90

[17] A.C. Larson, R.B. Von Dreele, GSAS-General Structure Analysis System. Report LAUR86–748, Los Alamos National Laboratory, Los Alamos, New Mexico, 1996.

[18] B.H. Toby
J. Appl. Crystallogr., 34 (2001), pp. 210–213

[19] P. Thomson, D.E. Cox, J.B. Hastings
J. Appl. Crystallogr., 20 (1987), pp. 79–83

[20] R. Miletich, D.R. Allan, W.F. Kush
R.M. Hazen, R.T. Downs (Eds.), High-Temperature and High-Pressure Crystal Chemistry, 41, Reviews in Mineralogy and Geochemistry, Washington DC, USA (2000), pp. 445–519

[21] R.A. Forman, G.J. Piermarini, J.D. Barnett, S. Block
Science, 176 (1972), p. 284

[22] H.K. Mao, J. Xu, P.M. Bell
J. Geophys. Res., 91 (1986), pp. 4673–4676

[23] A.P. Hammersley, S.O. Svensson, M. Hanfland, A.N. Fitch, D. Häusermann
High Pressure Res., 14 (1996), pp. 235–248

[24] R.J. Angel
EOS-FIT V6.0. Computer Program
Crystallography Laboratory, Department of Geological Sciences, Virginia Tech, Blacksburg, USA (2001)

[25] F. Birch
Phys. Rev., 71 (1947), pp. 809–824

[26] L. Leardini, S. Quartieri, G. Vezzalini
Microporous Mesoporous Mater., 127 (2010), pp. 219–227

[27] S. Bordiga, I. Roggero, P. Ugliengo, A. Zecchina, V. Bolis, G. Artioli, R. Buzzoni, G. Marra, F. Rivetti, G. Spanò, C. Lamberti
J. Chem. Soc., Dalton Trans. (2000), pp. 3921–3929

[28] R. Arletti, O. Ferro, S. Quartieri, A. Sani, G. Tabacchi, G. Vezzalini
Am. Mineral., 88 (2003), pp. 1416–1422

[29] E. Fois, A. Gamba, G. Tabacchi, R. Arletti, S. Quartieri, G. Vezzalini
Am. Mineral., 90 (2005), pp. 28–35

[30] S. Ori, S. Quartieri, G. Vezzalini, V. Dmitriev
Am. Mineral., 93 (2008), pp. 53–62

[31] R. Arletti, S. Quartieri, G. Vezzalini
Am. Mineral., 95 (2010), pp. 1247–1256

[32] L. Leardini, S. Quartieri, A. Martucci, G. Vezzalini, V. Dmitriev
Z. Kristallogr. (2012) http://dx.doi.org/10.1524/zkri.2012.1477

[33] G.D. Gatta
Eur. J. Mineral., 17 (2005), pp. 411–421